



Direct Observation at Room Temperature of the Orthorhombic Weyl Semimetal Phase in Thin Epitaxial MoTe 2

Polychronis Tsipas, Sotirios Fragkos, Dimitra Tsoutsou, Carlos Alvarez, Roberto Sant, Hanako Okuno, Gilles Renaud, Athanasios Dimoulas

► To cite this version:

Polychronis Tsipas, Sotirios Fragkos, Dimitra Tsoutsou, Carlos Alvarez, Roberto Sant, et al.. Direct Observation at Room Temperature of the Orthorhombic Weyl Semimetal Phase in Thin Epitaxial MoTe 2. *Advanced Functional Materials*, 2018, 28 (33), pp.1802084. 10.1002/adfm.201802084 . hal-02014393

HAL Id: hal-02014393

<https://hal.science/hal-02014393>

Submitted on 14 Feb 2019

HAL is a multi-disciplinary open access archive for the deposit and dissemination of scientific research documents, whether they are published or not. The documents may come from teaching and research institutions in France or abroad, or from public or private research centers.

L'archive ouverte pluridisciplinaire **HAL**, est destinée au dépôt et à la diffusion de documents scientifiques de niveau recherche, publiés ou non, émanant des établissements d'enseignement et de recherche français ou étrangers, des laboratoires publics ou privés.

Dear Author,

Please correct your galley proofs carefully and return them no more than four days after the page proofs have been received.

Please limit corrections to errors already in the text; cost incurred for any further changes or additions will be charged to the author, unless such changes have been agreed upon by the editor.

The editors reserve the right to publish your article without your corrections if the proofs do not arrive in time.

Note that the author is liable for damages arising from incorrect statements, including misprints.

Please note any queries that require your attention. These are indicated with a Q in the PDF and a question at the end of the document.

Reprints may be ordered by filling out the accompanying form.

Return the reprint order form by fax or by e-mail with the corrected proofs, to Wiley-VCH : afm@wiley.com

Corrections should be made directly in the PDF file using the PDF annotation tools. If you have questions about this, please contact the editorial office. The corrected PDF and any accompanying files should be uploaded to the journal's Editorial Manager site.

To avoid commonly occurring errors, **please ensure that the following important items are correct** in your proofs (please note that once your article is published online, no further corrections can be made):

- **Names** of all authors present and spelled correctly
- **Titles** of authors correct (Prof. or Dr. only: please note, Prof. Dr. is not used in the journals)
- **Addresses** and **postcodes** correct
- **E-mail address** of corresponding author correct (current email address)
- **Funding bodies** included and grant numbers accurate
- **Title** of article OK
- All **figures** included
- **Equations** correct (symbols and sub/superscripts)

Author Query Form

WILEY

Journal ADFM
Article adfm201802084

Dear Author,

During the copyediting of your manuscript the following queries arose.

Please refer to the query reference callout numbers in the page proofs and respond to each by marking the necessary comments using the PDF annotation tools.

Please remember illegible or unclear comments and corrections may delay publication.

Many thanks for your assistance.

| Query No. | Description | Remarks |
|-----------|---|---------|
| Q1 | Please provide TOC keyword. | |
| Q2 | Please confirm that forenames/given names (blue) and surnames/family names (vermilion) have been identified correctly. | |
| Q3 | Please provide the highest academic title (either Dr. or Prof.) for all authors, where applicable. | |
| Q4 | Please provide department name for affiliation 2 and 3. | |
| Q5 | Please provide postal code for affiliations 2–4. | |
| Q6 | Please define all acronyms at their first appearance in the abstract, text and table of contents, respectively. Only expanded forms are allowed if the elements are cited only once in the article. | |

Author: Please confirm that Funding Information has been identified correctly.

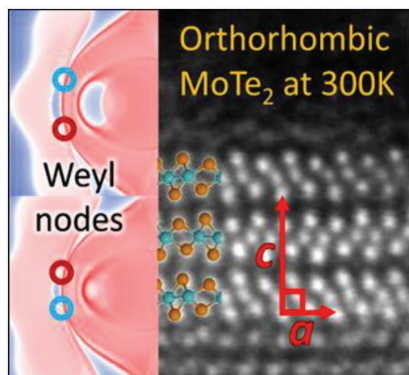
Please confirm that the funding sponsor list below was correctly extracted from your article: that it includes all funders and that the text has been matched to the correct FundRef Registry organization names. If a name was not found in the FundRef registry, it may not be the canonical name form, it may be a program name rather than an organization name, or it may be an organization not yet included in FundRef Registry. If you know of another name form or a parent organization name for a “not found” item on this list below, please share that information.

| FundRef Name | FundRef Organization Name |
|-------------------------------------|---------------------------|
| Greek State Scholarships Foundation | |
| French state funds | |
| CNRS | |

XXXX

P. Tsipas, S. Fragkos, D. Tsoutsou,
C. Alvarez, R. Sant, G. Renaud,
H. Okuno, A. Dimoulas* 1802084

**Direct Observation at Room
Temperature of the Orthorhombic
Weyl Semimetal Phase in Thin
Epitaxial MoTe_2**



The room temperature observation of the noncentrosymmetric orthorhombic phase of epitaxial MoTe_2 on $\text{InAs}(111)$ substrate is reported. Due to enlarged lattice parameters of 1–3 ML films a type II topological Weyl semimetal is predicted with Weyl nodes located a few meV below the Fermi level, accessible to transport.

Direct Observation at Room Temperature of the Orthorhombic Weyl Semimetal Phase in Thin Epitaxial MoTe₂

Polychronis Tsipas, Sotirios Fragkos, Dimitra Tsoutsou, Carlos Alvarez, Roberto Sant, Gilles Renaud, Hanako Okuno, and Athanasios Dimoulas*

The direct observation at room temperature of the noncentrosymmetric orthorhombic topological Weyl semimetal phase in epitaxial thin films of MoTe₂ grown on InAs(111)/Si(111) substrates by molecular beam epitaxy is reported. The orthorhombic phase is typically found at lower temperatures but its observation at room temperature in this work is attributed to the enlarged lattice parameters, influenced by the substrate, which stabilize an interlayer antibonding state compatible with the orthorhombic stacking. First-principles calculations predict eight type II Weyl nodes which are located below (but near) the Fermi energy making them accessible to charge transport and creating the prospect for practical applications exploiting the nontrivial topological properties. The orthorhombic phase coexists with an unconventional triclinic layer stacking which is different than the monoclinic or orthorhombic structures but it is centrosymmetric and topologically trivial.

1. Introduction

2D group VI (Mo,W) transition metal disulphide and diselenide materials, typically stabilized in the hexagonal 2H prismatic structure, are semiconductors and have been extensively studied due to their great potential for diverse and versatile applications.^[1–3] The Mo and W ditellurides (WTe₂ and MoTe₂) are notable exceptions because structural and electronic instabilities drive a transformation to a lower symmetry, distorted 1T (often referred to as 1T') octahedral crystal structure with metallic or semimetallic properties.^[4]

1T' is the most stable phase of WTe₂ at room temperature (RT). On the other hand, for MoTe₂ the most stable phase at RT is the 2H, while the 1T' is metastable lying only about a few tens of meV higher in energy.^[5] The small difference in energy allows the RT stabilization of 1T' utilizing bulk growth methodologies^[6–10] at high temperature typically followed by rapid cooling to RT. The metastability of 1T' implies that reversible transformations from the semiconducting to the metallic phase through a small energy barrier could be possible^[5] by applying external stimuli. This has already been demonstrated experimentally at RT by applying strain^[11] or electrostatic doping by a gate bias,^[12] rendering MoTe₂ a promising candidate material for the realization of useful electronic devices.

Moreover, MoTe₂ and WTe₂ exhibit exciting physical properties adding functionality and significantly extending the range of applications. In the limit of a monolayer with a centrosymmetric structure these materials have been predicted to be 2D topological insulators (or quantum spin Hall insulators)^[13] which have been experimentally verified recently for the case of WTe₂.^[14] In the few layer regime, 1T' WTe₂ adopts at RT an orthorhombic *Pmn*21(*T*_d) structure (γ -phase) which lacks inversion symmetry thus becoming a topological type II Weyl semimetal as first predicted^[15] and later verified^[16] for bulk WTe₂ material. On the other hand, few layer or bulk 1T' MoTe₂, at RT is typically found in a centrosymmetric monoclinic *P*21/*m* β -phase which is proposed to be a quantum spin Hall state.^[17] However MoTe₂ undergoes a structural phase transition from the β -phase to the noncentrosymmetric orthorhombic (*T*_d) γ -phase at lower temperatures, typically below 250 or 150 K, in which case MoTe₂ is predicted^[18] to become a type II topological Weyl semimetal (similar to γ -WTe₂), already verified by ARPES in bulk MoTe₂.^[8,9,19,20] The number of Weyl nodes, their position in *k*-space and energy, and the nature of surface states (topological or trivial) in γ -MoTe₂ depend sensitively on the lattice parameters and the strain. Theoretical values^[21] of the lattice parameters differ a lot depending on the density functional used and deviate from experimental values,^[6–9] which also depend a lot on the fabrication method. Most of the works find 8 Weyl nodes^[8,9,18,20,22] while for certain choice of small lattice parameters only 4 Weyl nodes are predicted,^[23] the

Dr. P. Tsipas, S. Fragkos, Dr. D. Tsoutsou, Dr. A. Dimoulas
National Center for Scientific Research "Demokritos"
15310 Athens, Greece

E-mail: a.dimoulas@inn.demokritos.gr

Dr. C. Alvarez, Dr. R. Sant, Dr. G. Renaud, Dr. H. Okuno
University Grenoble Alpes
Grenoble, France

Dr. C. Alvarez, Dr. G. Renaud, Dr. H. Okuno
CEA/INAC-MEM
Grenoble, France

Dr. R. Sant
Néel Institute
CNRS
Grenoble, France

DOI: 10.1002/adfm.201802084

lowest number ever reported for any Weyl semimetal. In all cases, MoTe_2 Weyl nodes^[8,9,18,20,22] are closer to Fermi energy (E_F) compared to WTe_2 ,^[15,16,24,25] however they are always above E_F , including those in $\text{Mo}_x\text{W}_{1-x}\text{Te}_2$,^[26,27] thus inhibiting both their observation by ARPES and their effective use in functional electronic devices.

To shed light on the electronic structure of $\gamma\text{-MoTe}_2$, the Weyl node configuration in particular, and to exploit the topological properties in practical applications, it is important to control the lattice parameter and to stabilize the γ -phase of MoTe_2 at RT by suitable epitaxial methods and substrates. More generally, the ability to epitaxially grow MoTe_2 thin films by synthetic methods on cm-scale crystalline substrates is essential to enable device processing. Epitaxial processes are typically nonequilibrium and are influenced by the substrate so the most stable structural phases, layer stacking, and physical properties of epitaxial thin films may be different compared to those produced by equilibrium bulk methodologies. In most cases, CVD-grown MoTe_2 thin films are found in the RT most stable 2H structure although $1\text{T}'$ structures are also obtained by postgrowth temperature treatments.^[28–30] Growing epitaxial thin films of MoTe_2 (and WTe_2) by MBE is challenging because Mo (W) and Te have very similar electronegativities^[31] so during coevaporation of Mo (W) and Te, the material tends to form intermetallic Mo–Mo or W–W bonds which do not favor the incorporation of Te in the material resulting in poor Te-deficient and highly nonstoichiometric films. Following the successful growth of the stable $1\text{T}'\text{-WTe}_2$ by MBE on a variety of 2D substrates by employing interrupted growth methodology,^[31] a few works^[32–34] have reported the stable 2H MoTe_2 phase by MBE but the metastable $1\text{T}'$ MoTe_2 phase was elusive until recently when two independent groups^[35,36] showed evidence of room temperature $1\text{T}'$ MBE films mixed with 2H on epi-graphene/SiC substrates.^[35] However, they lack of information about the epitaxial quality and the thin film structure; it is not known in particular whether they adopt the monoclinic ($\beta\text{-MoTe}_2$) or orthorhombic ($\gamma\text{-MoTe}_2$) structure. Stabilization of the latter Weyl semimetal phase is highly desirable but difficult to obtain at RT as already mentioned above. An interesting approach is to substitute $\approx 8\%$ of Mo by W to engineer the γ -phase as it has already been shown using bulk single crystals.^[37] Recently, indirect evidence of RT $\gamma\text{-MoTe}_2$ has been reported in thin films exfoliated from bulk where low dimensionality is thought to play a role.^[38] Direct observation of the $\gamma\text{-MoTe}_2$ phase at RT either on bulk or epitaxial material has not been reported.

In this paper we report on the direct RT observation of the important orthorhombic noncentrosymmetric Weyl semimetal γ -phase in epitaxial 3 ML MoTe_2 films grown layer by layer on $\text{InAs}(111)/\text{Si}(111)$ substrates by MBE. Moreover, we observe an unconventional triclinic layer stacking, which is however centrosymmetric, topologically predicted to be trivial with no Weyl points. The measured lattice constants of our epitaxial orthorhombic phase are found to be notably larger than the previously reported experimental values from bulk γ -phase MoTe_2 . We argue in this paper that the enlarged lattice parameters have important consequences on the energy position of the Weyl points as well on the stabilization of the γ -phase at room temperature in epitaxial thin films.

2. Results

2.1. Crystal Structure and Reciprocal Lattice

The structure details and the reciprocal lattice are described in brief to facilitate the data interpretation. As already mentioned, the 1T distorted ($1\text{T}'$) structure of MoTe_2 is typically found either in the RT monoclinic $P2_1/m$ β -phase or the low temperature ($T < 250$ K) orthorhombic (T_d) $Pmn2_1$ γ -phase (Figure 1). Here we use the notation as follows. $1\text{T}'$ refers to the distorted 1T without distinguishing between orthorhombic and monoclinic stacking. $T_d\text{-MoTe}_2$ refers to orthorhombic stacking while $\beta\text{-MoTe}_2$ refers to monoclinic stacking. A characteristic difference between the two phases is the interatomic distance d (Figure 1b,c) which becomes larger in the orthorhombic structure compared to the monoclinic ($d_o > d_m$) due to a parallel shift of the second (top) layer with respect to the bottom one.^[21] The undistorted 1T lattice can be described either by a primitive hexagonal unit cell (solid lines in Figure 1d) or by a rectangular surface nonprimitive unit cell (dashed line) which is double the hexagonal primitive unit cell (solid line), with lattice parameters a_T and b_T such that $a_T/b_T = \sqrt{3}$. On the other hand, the surface rectangular primitive unit cell of $1\text{T}'$ has $a_{T'}/b_{T'} > \sqrt{3}$ deviating from the “ideal” value of $\sqrt{3}$. Similarly, the reciprocal space or $1\text{T}'$ (Figure 1e) has a rectangular primitive unit cell with the reciprocal lattice constant ratio $b^*_{T'}/a^*_{T'} > \sqrt{3}$. The deviation of these ratios from ideal values produces characteristic signatures in our data as will be discussed below facilitating the nanostructure characterization of our films.

2.2. Sequential Layer by Layer Thin Film Epitaxial Growth and Surface Structure

In-terminated $\text{InAs}(111)/\text{Si}(111)$ substrates are prepared by ex situ chemical cleaning followed by in situ thermal annealing and, where required, by a mild Ar^+ sputtering (see the Experimental Section) prior to annealing, until a 2×2 reconstruction pattern is obtained in reflection high energy electron diffraction (RHEED) (Figure S1, Supporting Information), indicative of a clean, oxide-free surface. Thin 1–3 ML MoTe_2 films are grown (see the Experimental Section) in a layer-by-layer sequence, with each layer grown in a two-step process. First, a single layer MoTe_2 is grown at a low temperature of 280°C and Te/Mo ratio of 100/1, adopting a beam-interrupted epitaxy method similar to that used for the MBE growth of WTe_2 .^[31] After 30 s of W and Te codeposition, the growth is interrupted by closing the Mo shutter for about 60 s, while the film is continually exposed to Te and then the growth continues again by opening the Mo shutter for another 30 s. The process is repeated until 1 ML of MoTe_2 is completed. The growth rate is estimated to be 0.5 ML min^{-1} . Subsequently, the sample is annealed at 400°C in the presence of Te flux (0.5 \AA s^{-1}) for 30 min to improve the crystallinity and the surface ordering monitored by RHEED (Figure S1, Supporting Information). Once the first layer is fully formed and optimized, the second and third layers are grown by repeating the same process, thus enabling the sequential layer-by-layer growth of MoTe_2 thin films.

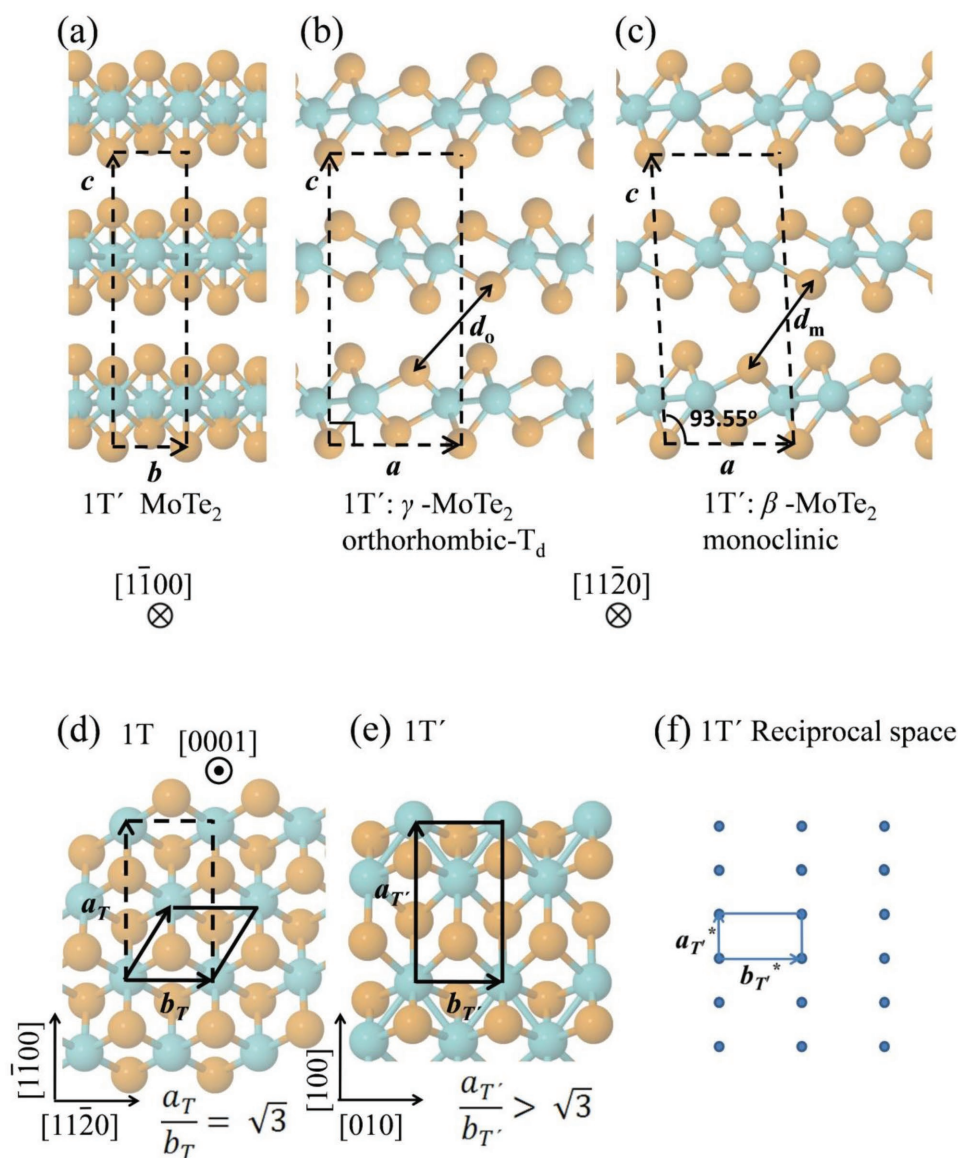


Figure 1. Crystal phases for the 1T distorted (1T') MoTe₂ a) along [1 $\bar{1}$ 00] direction and b) orthorhombic T_d-phase along the [1 $\bar{1}$ 20] direction, c) monoclinic β -phase along the [1 $\bar{1}$ 20] direction. d–f) Top view of the direct and reciprocal lattices. Lattice parameters are indicated as a , b (direct) and a^* , b^* (reciprocal): (d) 1T, (e) 1T', (f) 1T' reciprocal lattice. The solid lines represent the primitive unit cells. The broken line represents the nonprimitive unit cell for 1T [1 $\bar{1}$ 00] and [1 $\bar{1}$ 20] of 1T correspond to [100] and [010] of the distorted (1T') lattice, respectively.

The surface nanostructure of 1 ML 1T' MoTe₂ is imaged in Figure 2a by in-situ ultrahigh vacuum scanning tunneling microscopy (UHV-STM) at RT. The domains have an average lateral size ≈ 40 nm and they differ in height about 3.5 Å (Figure 2b), which is the same as the height of monoatomic steps of the underlying InAs substrate. It is therefore concluded that the domain formation in MoTe₂ originates from the monatomic step nanostructure of the InAs surface, consistent with scanning transmission electron microscopy (STEM) observations shown in subsequent section (Figure 3). Deposition of a second layer results in the formation of 2D islands (Figure 2c) with a height of ≈ 7 Å (Figure 2d) which is roughly equal to the thickness of a single 1T' MoTe₂ layer including the van der Waals gap between the top and the

bottom layers. The islands coalesce to form a complete second layer.

Atomic resolution STM images of a single domain are consistent with the symmetry of 1T' MoTe₂ surface (Figure 2e). The Fourier transform in Figure 2f yields the surface reciprocal space in similarity with the schematic of Figure 1f. In a different part of the surface, two domains A and B rotated 60° with each other are imaged (Figure 2g) resulting in a more complex reciprocal space (see the Fourier transform of Figure 2h) where additional periodicities (1 and 2 in Figure 2h), define a reciprocal lattice for domain B (white dashed rectangles) rotated by 60° with respect to the one corresponding to domain A (red dashed rectangles). Consideration of the complex reciprocal space composed of superimposed rotated lattices is essential

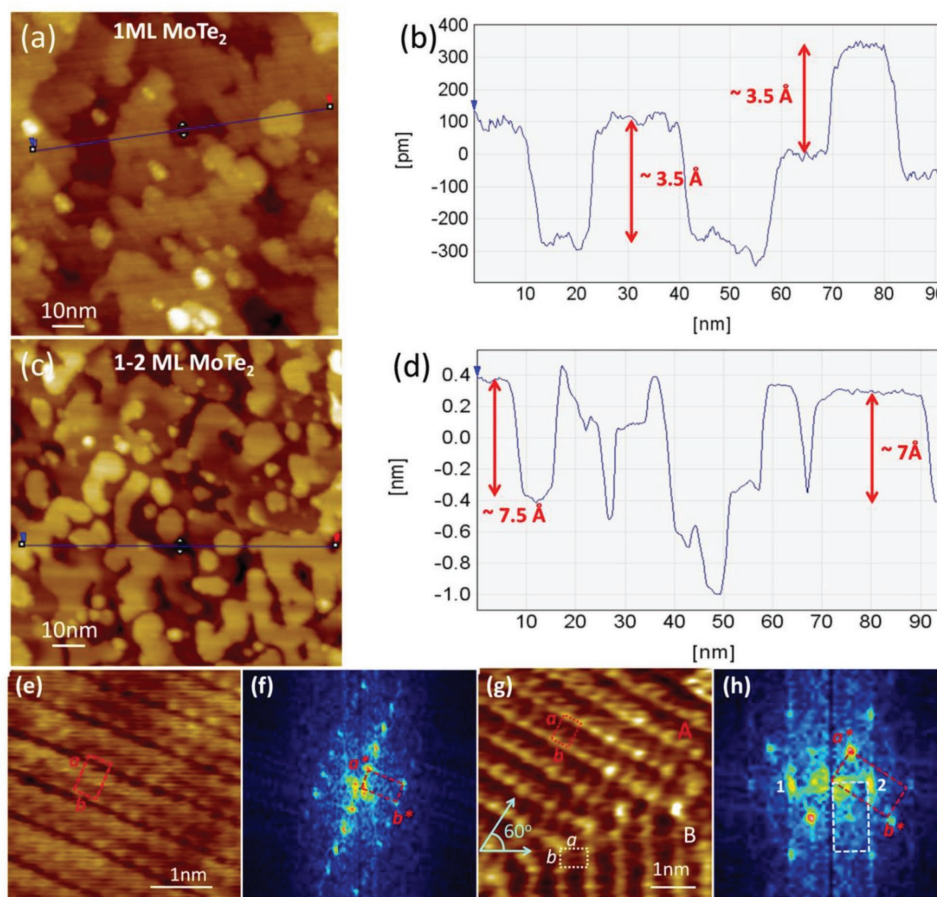


Figure 2. In situ room temperature UHV-STM of 1T'-MoTe₂. a,b) 1 ML MoTe₂ and the corresponding line scan, showing the influence of the substrate. c,d) Surface morphology after the deposition of an incomplete second layer MoTe₂ and the corresponding linescan showing the thickness of the top layer of about 7 Å, including the van der Waals gap with the bottom layer. e,f) Surface and Fourier pattern showing a single domain 1 ML 1T'-MoTe₂. The dashed rectangles show the unit cells of real (e) and reciprocal space (f) lattices. g) Image of two domains A and B rotated by 60° between each other h) The additional intense spots marked by 1 and 2 originate from the rotated pattern B and defines the superimposed reciprocal lattice (white dotted rectangles).

for the interpretation of X-ray diffraction (XRD), angle resolved photoelectron spectroscopy (ARPES) and RHEED measurements reported in the subsequent sections and the Supporting Information.

2.3. Orthorhombic and Unconventional Triclinic Layer Stacking Structure

The MoTe₂ thin films are evaluated in cross-section by STEM at RT to identify the film layer stacking. Figure 3 shows cross-section images for both 1 and 3 ML MoTe₂. In Figure 3a, two regions of 1 ML of 1T' MoTe₂ are shown interrupted by an atomic step in the InAs, ≈ 3.5 Å, hence forming domains with different heights, similar to STM observations in Figure 2a. It is worth mentioning that there is no evidence for the 2H prismatic phase which is the most stable at RT, therefore the thin films are in a pure 1T' phase.

As the growth continues from 1 to 3 ML 1T' MoTe₂, two dominant phases are observed, namely the orthorhombic T_d-MoTe₂ phase (Figure 3c), comprising two layers in the unit

cell, which typically appears at lower temperatures (<250 K) and an unconventional triclinic stacking, containing one layer per unit cell (Figure 3e), not previously reported. A fundamental difference between the triclinic stacking of Figure 3e and the conventional room temperature stable β -MoTe₂ monoclinic phase is that the second layer is rotated by 180° with respect to the first layer. The lattice parameter along the *c*-axis in the T_d orthorhombic structure (Figure 3b,c) is measured to be between 14.1 and 14.2 Å (Figure 3d), which is significantly larger than the reported experimental *c* values from bulk T_d-MoTe₂ crystals^[6–9] found to be in the range between 13.861 and 13.8935 Å. Moreover, among the different 1T' structures (Figure 1), the most stable room temperature monoclinic stacking, known as β -MoTe₂ (Figure 1c) is absent in our films. Additionally, fast Fourier transform (FFT) patterns were calculated from the regions containing only the MoTe₂ film in the STEM images; they are shown in Figure 3f–h. The FFT patterns were analyzed and compared with corresponding simulated electron diffraction patterns to verify the different MoTe₂ crystals structures. The simulated electron diffractions patterns and this analysis are presented in Figure S3 of the Supporting Information.

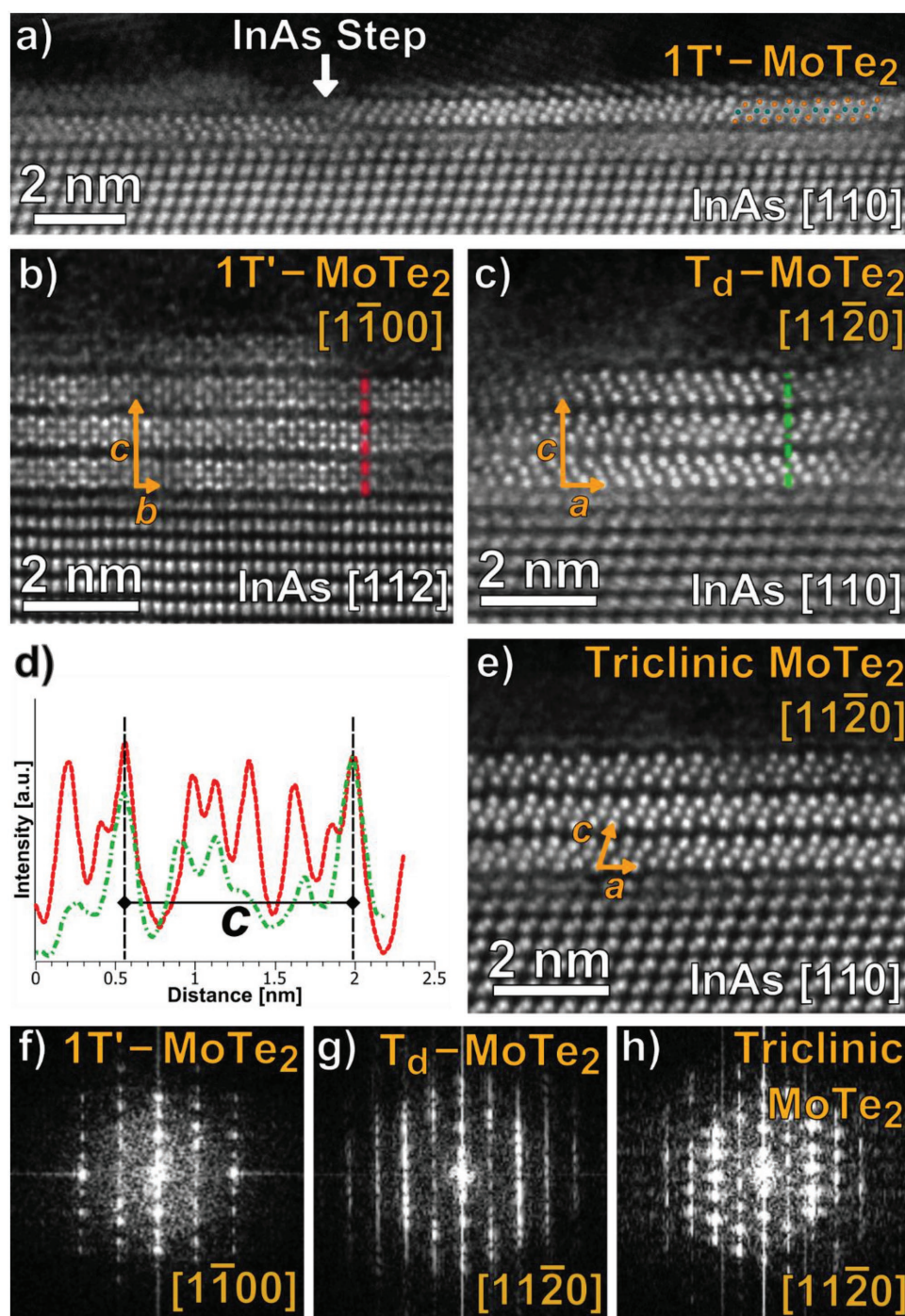


Figure 3. STEM images from epitaxial MoTe_2 thin films. a) 1 ML of $1\text{T}'$ MoTe_2 showing film interruption at the edge of an InAs monoatomic step b) 3 ML $1\text{T}'$ phase along $[1\bar{1}00]$ zone axis, c) 3 ML orthorhombic (T_d) stacking along $[11\bar{2}0]$ zone axis, d) intensity line plot in the c direction from images (b) and (c) in red and green, respectively, e) 3 ML of unconventional triclinic stacking along $[11\bar{2}0]$ zone axis. f–h) FFT patterns from respective STEM images. The equivalent $[uvw]$ notation for the zone axis directions are $[100]$ for $[1\bar{1}00]$, and $[010]$ for $[11\bar{2}0]$.

2.4. In-Plane Epitaxial Orientation and Rotated Domain Microstructure Investigated by Synchrotron Grazing Incidence X-Ray Diffraction (GIXD)

Single-layer and three-layer MoTe_2 are evaluated by GIXD and the data for 3 ML films are presented in Figure 4. The in-plane

reciprocal space map (RSM) in Figure 4a reveals that the MoTe_2 film is epitaxially grown on InAs in such a way that $[100]_{\text{MoTe}_2} // [11\bar{2}]_{\text{InAs}}$, and $[010]_{\text{MoTe}_2} // [01\bar{1}]_{\text{InAs}}$ in the plane. We observe no 30° or 90° rotated domains or polycrystallinity other than that arising from the Al protecting cap (rings in Figure 4a). The positions of the diffraction peaks in k -space are in agreement

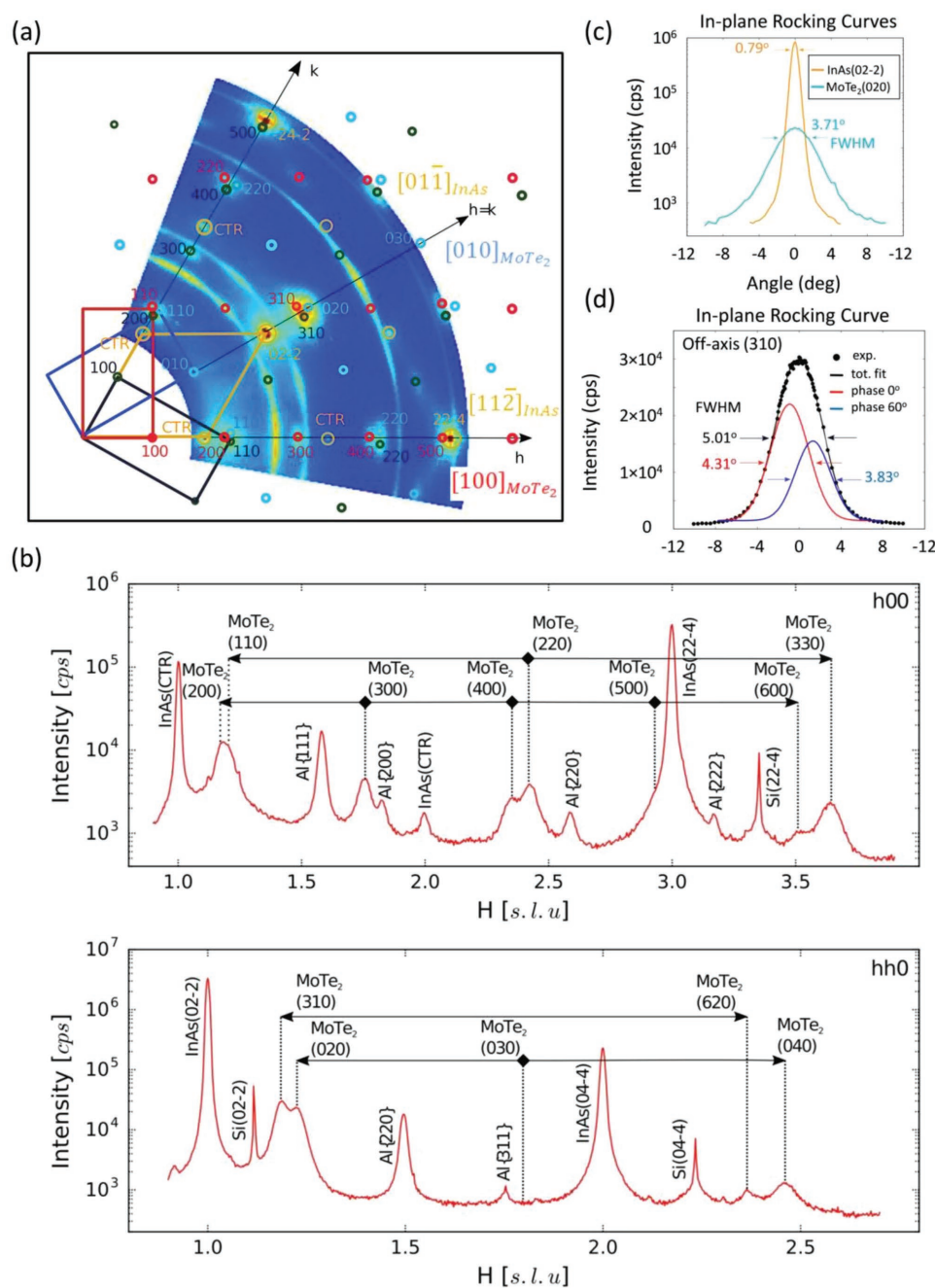


Figure 4. Synchrotron GIXD from epitaxial 3 ML MoTe_2 a) reciprocal space map (RSM). The diffraction peak and crystallographic orientations correspond to bulk Miller indices notation. The h , k and $h = k$ axis are high symmetry directions in hexagonal surface k -space. The open circles and rectangles denote reciprocal lattice points and unit cells, respectively, originating from three rotated domains: 0° (red), 60° (blue), 120° (black). CTR denotes crystal truncation rods. Polycrystalline rings are due to Al cap layer b) Radial scans along the h and $h = k$ crystallographic directions shown in (a). c) In-plane rocking curves of the on-axis (020) single peak and d) the off-axis (310) peak (symbol curve) deconvoluted into two peaks (solid blue and red lines) originating from two different domains rotated by 60° .

with a complex reciprocal space (open circles in Figure 4a) which is a superposition from 0° , 60° , and 120° rotated domains. The most characteristic configuration is the triplet along $h = k$ ($[01-1]_{\text{InAs}}$) consisting of the on-axis (020) peak and the two off-axis (310) peaks all belonging to different domains rotated between each other by 60° . It should be noted that in the ideal case where $b^*/a^* = \sqrt{3}$ applying to the hexagonal

symmetry of the undistorted 1T structure (see Figure 1d), all three closely spaced reciprocal lattice points would be expected to coincide giving a single diffraction peak. In our case though of a distorted 1T' MoTe_2 lattice, where the ratio deviates from ideal ($b^*/a^* > \sqrt{3}$), the peak splitting into a triplet configuration is clearly detected by GIXD (Figure 4a). Similar situation arises along h ($[11-2]_{\text{InAs}}$) direction with the triplet consisting of

the on-axis (400) peak and two off-axis (220) peaks from rotated domains as well as the triplet involving (200) and two (110) peaks although the latter triplet is not resolved very well. As a consequence, the radial scans along h and $h = k$ directions in Figure 4b show doublets for certain diffractions.

In the doublet the peak due to the off axis signals superposition have larger transversal width as seen from the rocking curves of Figure 4c and d because they have the contributions from two off-axis diffraction peaks (see the deconvolution of (310) diffraction peak in Figure 3d). From the FWHM of the on-line single peak (020) in Figure 3c an in-plane mosaicity of 3.71° is estimated which is substantially higher than that of the InAs substrate (0.79°); also higher than the mosaicity of 1.79° observed in epitaxial ZrTe_2 on InAs(111) substrate.^[39]

Considering only the well resolved on-axis single peaks (020), (300), and (400), the reciprocal (a^* , b^*) and direct (a , b) lattice parameters can be accurately determined from the RSM and the radial scans as follows. The position of the 020 peak in the q space is $q = 3.5894 \text{ \AA}^{-1}$ and it is equal to two times the reciprocal space unit cell lattice constant b (Figure 4b). Therefore $b^* = q/2 = 1.7947 \text{ \AA}^{-1}$ and $b = 2\pi/b^* = 3.501 (\pm 0.003) \text{ \AA}$. Looking along the h and k directions in Figure 4a, the (300) and (400) peaks are $3a^*$ and $4a^*$, respectively, and by considering their location in k -space from Figure 4b, $a^* = 0.99105 \text{ \AA}^{-1}$ (averaged over the four peaks, two along each direction h and k) and $a = 2\pi/a^* = 6.340 (\pm 0.005) \text{ \AA}$ are obtained. These values are in reasonably good agreement with the ones deduced from RHEED (Figure S1, Supporting Information).

It is worth noting that the values a , b (determined from GIXD) and c (determined from STEM) in our epitaxial thin films are larger than the ones measured from bulk T_d - MoTe_2 crystals.^[6–9] This is attributed to the influence of the substrate and the layer-by-layer sequential growth adopted in the present work.

2.5. Electronic Band Structure of 1T' MoTe_2 Epitaxial Thin Films

The electronic band structure of 1 ML 1T' MoTe_2 imaged by in situ ARPES is given in Figure 5, in direct comparison with 1 ML density functional theory (DFT) first-principles calculations using the experimental lattice parameters deduced from our epitaxial thin films. In contrast to exfoliated single crystal 1T' MoTe_2 , our epitaxial material contains rotated domains differing by 60° between each other (see also discussion of STM, XRD, and RHEED in Figures 2 and 4 and Figure S1, Supporting Information). This gives rise to a complex Brillouin zone (BZ) configuration (Figure 5d) resulting in an overlap of the electronic band structure along two different directions in the BZ, as for example ΓY and ΓS directions, in the ARPES spectrum of Figure 5a, yielding a complex dispersion adversely impacting energy and momentum resolution. By employing second derivative of the energy dispersion the resolution is improved (Figure 5b,c) yielding a reasonably good agreement with DFT simulations along the high symmetry lines in the BZ which are indicated by thick (blue and red) arrows in Figure 5d. Notably, the feature at around $k_{\parallel} \approx 1 \text{ \AA}^{-1}$ in Figure 5b is located at the Γ point of the neighboring BZ (indicated by broken line in Figure 5d) and is effectively a replica of the band at $k_{\parallel} = 0 \text{ \AA}^{-1}$.

There is also evidence for the existence of electron pockets near the Γ point along ΓX as predicted by DFT in Figure 5c (blue line).

In principle, by applying ARPES to thicker films, it should be possible to distinguish between orthorhombic T_d -phase and triclinic stacking and therefore identify the most dominant configuration however the ARPES spectra for 2 and 3 ML (not shown here) are very similar to the ones for 1 ML (Figure 5). This could be explained by considering that 21.22 eV ARPES known to be a surface sensitive technique probes the topmost layer which is coupled weakly to the bottom layers showing the behavior of a single layer in ARPES.

Using the measured set of lattice parameters in our epitaxial thin films ($a = 6.340 \text{ \AA}$, $b = 3.501 \text{ \AA}$, $c = 14.15 \text{ \AA}$) we have performed DFT bulk band structure calculations for the noncentrosymmetric orthorhombic (T_d) structure with the aim to predict the existence of Weyl nodes and find their location in energy and k -space. By considering the topmost valence band and the next (conduction) band we find eight Weyl nodes as a result of broken inversion symmetry (Figure 6), which are all located in the $k_z = 0$ plane and are symmetrically placed in k -space with respect to the high symmetry directions $X-\Gamma-X$ and $Y-\Gamma-Y$ as shown in the schematic of Figure 6a. Their exact coordinates in k -space and energy are as follows: $W1^-$: ($k_x = 0.18707 \text{ \AA}^{-1}$, $k_y = 0.0456 \text{ \AA}^{-1}$, $k_z = 0 \text{ \AA}^{-1}$) at $E-E_F = -1.1 \text{ meV}$, $W2^+$ ($k_x = 0.1871 \text{ \AA}^{-1}$, $k_y = 0.0351 \text{ \AA}^{-1}$, $k_z = 0 \text{ \AA}^{-1}$) at $E-E_F = -12.9 \text{ meV}$. The Weyl nodes in each pair have opposite chirality and are located below the Fermi level but very close to it (Figure 6b). The Fermi arc connecting the Weyl nodes with opposite chirality (+, −) is shown as part of the surface state passing through them in Figure 6b. It should be noted that this set of lattice parameters deduced from our epitaxial thin films yields Weyl nodes which are closer to the Fermi level than any other reported^[8,9,18,20,23,24] Weyl nodes for MoTe_2 in the literature. While in all of these cases, they are typically located a few tens of meV above E_F , in our epitaxial thin films the Weyl nodes are predicted just below the Fermi level which facilitates observations by ARPES and makes them accessible to transport, thus suitable for electronic applications where topological properties can play a critical role.

The unconventional triclinic layer stacking as evidenced by STEM in Figure 3d, yields a calculated bulk band structure (Figure S4, Supporting Information) with no Weyl points, a result which is expected since this structure is centrosymmetric.

To gain more insight about the possible role of the enlarged lattice parameters on the stabilization of the orthorhombic T_d -phase at room temperature in our epitaxial thin films we analyze our first-principles calculations which have been performed using two different sets of experimental lattice parameters (Figure 7) following similar methodology and reasoning as in ref. [21] Set #1 ($a = 6.3341 \text{ \AA}$, $b = 3.4751 \text{ \AA}$, $c = 13.8816 \text{ \AA}$) in Figure 7a is an average obtained from experimentally reported values for bulk, free standing T_d - MoTe_2 ,^[6–9] detected at low temperatures and Set #2 ($a = 6.340 \text{ \AA}$, $b = 3.501 \text{ \AA}$, $c = 14.15 \text{ \AA}$) in Figure 7b is from our measured T_d - MoTe_2 epitaxial films at RT. In both band structures (Figure 7a,b), the uppermost valence band B1 along ΓA consists of hybridized Te p_x and Mo d_{xz} orbitals while the lower band B2 consists of hybridized Te p_z and Mo d_{z^2} orbitals. From the plot of the wavefunctions of B1 and B2 at Γ for Set #2 (our experimental

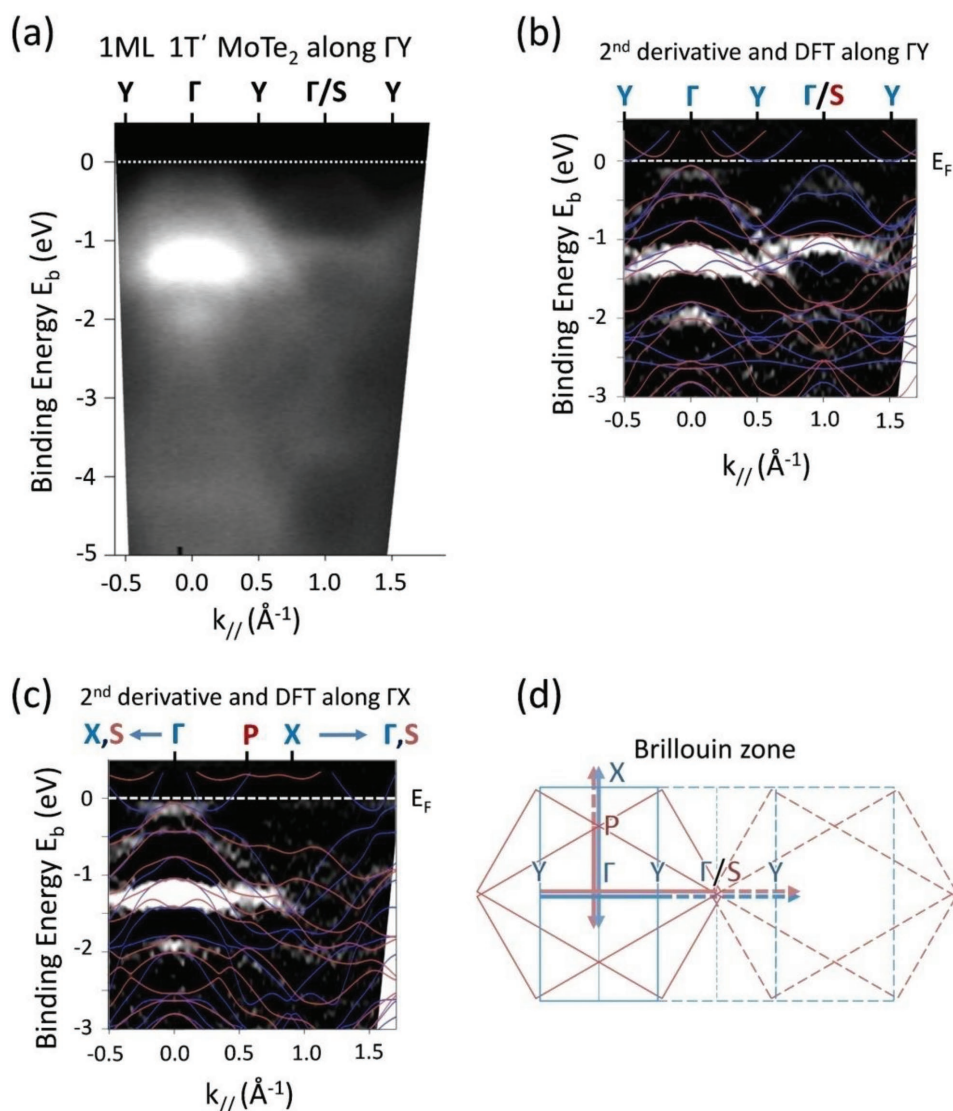


Figure 5. a) Electronic band structure of 1 ML 1T' MoTe₂ imaged by ARPES at room temperature a) ARPES along ΓY , b) 2nd derivative of spectra in (a) compared with DFT simulations for 1 ML 1T' MoTe₂. Blue line is along ΓY , red line is along ΓS c) 2nd derivative of spectra along ΓX compared with DFT simulations for 1 ML 1T' MoTe₂. e) Schematic illustration of k -space constructed by the superposition of orthorhombic Brillouin zones (BZ) originated from of 0° (blue solid line) 60° or 120° rotated domains (red solid lines). The dashed lines denote neighboring Brillouin zones. The Γ point of the neighboring 0° BZ nearly coincides with the S point of the rotated BZs. The horizontal thick arrows shows the paths along which the ARPES spectra in (a) and (b) are recorded. Note that ARPES images simultaneously the bands along ΓY (blue arrow) and ΓS (red arrow) paths since these two paths are parallel due to the overlapping of rotated domains. The thick vertical arrow shows the paths along which the ARPES in (c) is recorded.

parameters) in Figures 7c,d, it is inferred that interlayer coupling occurs through an antibonding configuration along interlayer distance d between inner Te atoms having large and opposite sign wavefunction values. Since B2 is fully occupied in both cases the degree of occupancy of the interlayer antibonding band B1 along ΓA and near Γ determines the tendency of MoTe₂ to stabilize in the T_d phase. For Set #1 of the experimental bulk parameters obtained from the literature (Figure 7a; Figure S4, Supporting Information), a significant portion of the uppermost valence band B1 near Γ point along ΓA is unoccupied. In contrast, for Set #2 of our epitaxial thin film enlarged experimental parameters in Figure 7b, B1 is fully occupied thus strengthening the interlayer antibonding state which favors

an elongated interlayer distance d (Figure 7c). This elongation stabilizes T_d stacking configuration at RT since $d(=d_0)$ for orthorhombic stacking is large and indeed larger than the corresponding monoclinic distance d_m (see Figure 1b,c).

3. Discussion

In this work we use MBE to grow the distorted 1T (1T') phase of MoTe₂ epitaxially on InAs(111)/Si(111) substrates. Adopting an interrupted growth methodology at low growth temperatures (≈ 280 °C) first applied to the MBE growth of WTe₂ on MoS₂ and HOPG substrates,^[31] we show by STEM and GIXD that a

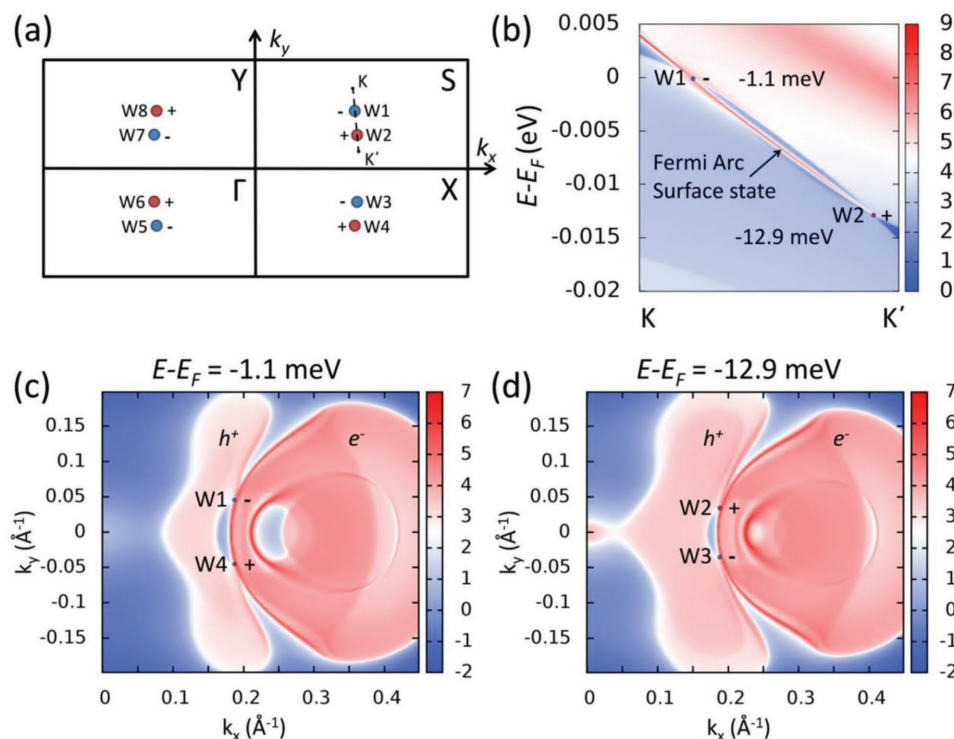


Figure 6. Calculated Weyl node configuration for the bulk orthorhombic T_d -MoTe₂ using the experimental parameter sets deduced from our epitaxial films a) Positions of Weyl nodes in the first Brillouin zone. The blue and red points closely spaced between each other indicate pair of Weyl nodes with opposite chirality. b) Theoretical energy dispersion along a path KK' shown by broken line in (a), passing through the pair of Weyl points. Theoretical constant energy contour plots for two different energies c) $E = -1.1$ meV and d) $E = -12.9$ meV corresponding to the energy location of the Weyl node pairs. e^- and h^+ denote the touching electron and hole pockets, respectively.

pure 1T' MoTe₂ phase can be obtained with improved crystallinity after postgrowth annealing at 400 °C. Despite the fact the 2H prismatic phase of MoTe₂ is more stable at RT, a pure 1T' MoTe₂ phase is observed here attributed to the influence of the substrate due to tensile biaxial strain and/or electron doping. Tensile strain between 0.3% and 3% under uniaxial conditions as theoretically predicted^[5] or 0.2% as experimentally demonstrated^[11] is thought to drive the transition from the stable 2H to the metastable 1T' MoTe₂ phase at or near RT. In our case, the in-plane a and b lattice parameters of the epitaxial films are accurately measured by synchrotron GIXD (Figure 4) and found to be larger than those obtained in free standing films exfoliated from bulk,^[6,9] indicating a relatively small epitaxial tensile strain configuration with $\varepsilon_{xx} = \delta a/a \approx +0.1\%$ and $\varepsilon_{yy} = \delta b/b \approx +0.7\%$, which may partly explain the transformation to 1T' phase at RT in our epitaxial thin films. It has also been predicted^[17] that electron doping $\approx 0.1e^-$ per unit cell induces the 2H \rightarrow 1T' transition in MoTe₂. Electron doping could be a possible scenario in our case, since the electronic charge can be provided by the InAs substrate which is known to have strong n-type semiconductor character at the surface due to the accumulation of a dense electron gas.^[40]

MBE, a typically far from equilibrium process, can produce thin film structures which cannot be obtained under equilibrium conditions. Beyond the substrate effects (strain, doping) already discussed above, the ability to sequentially grow one layer on top of another as in the present work, allows different stacking configurations which cannot be obtained in films

exfoliated from bulk. Such a layer stacking, namely a triclinic structure is observed here by STEM (Figure 3e; Figure S2, Supporting Information), where all layers are in phase presenting a fundamental difference compared to the typical monoclinic or orthorhombic structures where two consecutive layers are 180° out of phase (Figure 1). Hints of such in-phase layer stacking are found also in MBE-grown WTe₂^[31] but not sufficiently emphasized. Although the triclinic structure is centrosymmetric with trivial topology (no Weyl nodes found), it is very interesting that here the important noncentrosymmetric orthorhombic (T_d) Weyl semimetal phase is observed by STEM coexisting with the triclinic structure. This orthorhombic phase is typically reported in the literature below 250 or 150 K so questions are raised about the possible origin of its stability at RT as observed in our work. The reduced dimensionality analysis previously proposed to explain the indirect observation^[38] of RT T_d -MoTe₂ in 12 nm thick films exfoliated from bulk does not directly apply to our ultrathin (1–3 ML) films. Our DFT analysis for T_d -MoTe₂ (Figure 7) shows that the enlarged lattice parameters of our epitaxial thin films result in a characteristic band structure where the uppermost valence band B along ΓA is fully occupied dispersing well below the Fermi level similar to what is observed for T_d -WTe₂.^[21] It should be noted that in the case of T_d -WTe₂, the full occupation of this band is correlated with the absence of a barrier in the energy profile for the transition from β to T_d -phase^[21] which explains the stability of T_d -phase at RT. A similar situation could apply for the epitaxial MoTe₂ in this paper. Expressing it in a different way, it

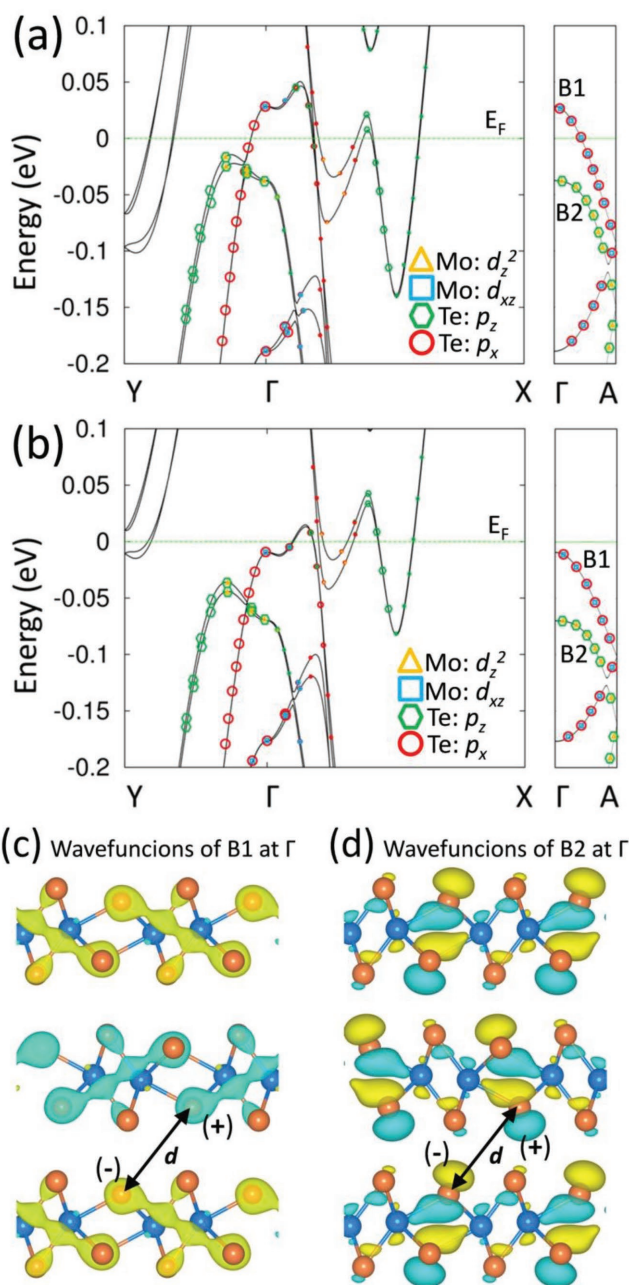


Figure 7. DFT calculations for bulk T_d -MoTe₂ for two different lattice parameter sets: a) averaged experimental lattice parameters from bulk T_d -MoTe₂ taken from refs. [6–9], b) experimental lattice parameters from epitaxial thin films in this work. The symbols in both (a) and (b) represent the projections of the bands in the Te and Mo orbitals. c,d) Wavefunctions at the Γ point are plotted for valence bands B1 and B2, respectively, corresponding to T_d -MoTe₂ calculated with the experimental parameters reported in this work (Set #2). The wavefunction sign (+) and (–) is indicated by blue and green color, respectively.

can be said that this fully occupied band B (Figure 7) is related to an antibonding state^[21] along the interlayer distance d (see Figure 1), then the T_d -MoTe₂ is favored because this phase is compatible with an enlarged d ($d_o > d_m$ in Figure 1) as it would be expected for an antibonding state. This analysis shows that

the enlarged lattice parameters in the epitaxial thin films could explain the observation at RT of the orthorhombic T_d -MoTe₂ instead of the monoclinic phase.

The RT orthorhombic MoTe₂ reported here lacks inversion symmetry so it is expected to be a topological Weyl semimetal. Using the enlarged experimental lattice parameters found in this work, a DFT analysis (Figure 6) for the T_d -MoTe₂ predicts eight type II Weyl nodes which are located very close to the Fermi level and just below it, in notable difference with previous results where all Weyl points were found above E_F . The occupation of states near the Weyl nodes makes them visible in ARPES electronic band imaging and accessible to transport which means that epitaxial thin films of T_d -MoTe₂ on InAs(111) substrates can be used to fabricate devices which could exploit the nontrivial topological properties of these films in practical RT applications.

Future work should focus on improving the epitaxial quality of these films. Although there is a very good in-plane epitaxial alignment between MoTe₂ and InAs substrate such that $[100]_{\text{MoTe}_2} // [11-2]_{\text{InAs}}$, and $[010]_{\text{MoTe}_2} // [01-1]_{\text{InAs}}$ (Figure 4), with no signs of polycrystallinity, the in-plane mosaicity of 3.71° is substantially higher than the InAs one (0.79°) and higher than the 1.79° mosaicity of epitaxial ZrTe₂ on InAs.^[39] Moreover, the MoTe₂ epilayer, similar to the case of ZrTe₂,^[39] follows the landscape of the InAs surface (STEM in Figure 3) which shows monatomic steps of 3.5 Å, producing a MoTe₂ nanostructure with domain size in the order of a few tens of nm as also seen by STM in Figure 2. The presence of 60° and 120° rotated domains is widely evidenced by STM, RHEED, and GIXD data, which is a distinct characteristic of our thin epitaxial films compared to single crystals obtained from bulk where such domains are absent. While these rotated domains in the hexagonal undistorted 1T or 2H MoTe₂ structure are equivalent, in 1T' MoTe₂ result in a complex k -space and Brillouin zone, mixing the energy dispersion along different directions thus adversely affecting resolution, inhibiting clear observation of Weyl node configuration in ARPES. Domain rotation may be facilitated at the step edges, where also the continuity of the film may be interrupted (Figure 3), which could be harmful for electrical transport. By improving the surface treatment of InAs prior to growth we may be able to minimize the density of monatomic steps and increase the domain size in an attempt to obtain a single crystalline epitaxial film. Although the use of single crystal InAs(111) could resolve some of the issues related to the step and domain formation and improve the mosaicity of MoTe₂, the effort should focus on the improvement of epitaxial InAs on Si substrates since the availability of large area wafers (200 and 300 mm) of this kind is essential for a manufacturable technology of MoTe₂ and other 2D materials in the future.

4. Conclusion

In this work epitaxial thin films of MoTe₂ with the distorted 1T' structure are grown by molecular beam epitaxy on InAs(111)/Si(111) substrates. The films are rotationally commensurate with the substrate such that $[100]_{\text{MoTe}_2} // [11-2]_{\text{InAs}}$ and $[010]_{\text{MoTe}_2} // [01-1]_{\text{InAs}}$ although 60° and 120° rotational domains are present, detected by STM, synchrotron GIXD, and RHEED.

Using STEM cross-sectional measurements in 3 ML MoTe₂ we identify two different phases coexisting in the layer. The first phase shows an orthorhombic (*T_d*) stacking (or γ -MoTe₂) and the second phase is a triclinic stacking not reported before. From GIXD and STEM we measure lattice parameters values $a = 6.340$ Å, $b = 3.501$ Å and out of plane parameter for the orthorhombic *T_d*-phase $c = 14.1$ – 14.2 Å which are larger compared to freestanding thin films exfoliated from bulk as a result of the influence from the substrate.

The MoTe₂ orthorhombic *T_d*-phase typically found at temperatures lower than 250 K, here is observed at room temperature which is attributed to an interlayer antibonding state compatible with the orthorhombic *T_d*-phase as a result of the enlarged lattice parameters of our epitaxial thin films. The orthorhombic *T_d*-MoTe₂ is noncentrosymmetric yielding a topological type II Weyl semimetal phase. Eight Weyl nodes calculated by DFT a few meV below the Fermi level are accessible to transport creating the prospect for room temperature electronic applications where the topologically nontrivial properties of MoTe₂ epitaxial layers could play a role.

5. Experimental Section

Surface Preparation and Film Growth Details: The InAs(111)/Si(111) substrates were chemically cleaned in a 5N HF solution in isopropyl alcohol for 5 min to etch the surface oxide and subsequently rinsed in isopropyl alcohol for 30 s in order to avoid reoxidation of the substrate. An annealing step at 400° C in UHV follows to get a clean and flat InAs(111) surface as evidenced by RHEED (Figure S1, Supporting Information) and X-ray photoelectron spectroscopy. Where appropriate, mild Ar⁺ sputtering was used ($E \approx 1.5$ keV, $p \approx 2 \times 10^{-5}$ mbar, $t \approx 30$ s) prior the annealing step to obtain a clean surface as evidenced by a 2×2 reconstruction in RHEED pattern (Figure S1a,b, Supporting Information) attributed to In surface vacancies.^[41]

ARPES Measurements: In-situ ARPES was conducted at room temperature in a μ -metal analytical chamber equipped with a 100 mm hemispherical electron analyzer (SPECS PHOIBOS 100) and a 2D CCD detector. The energy resolution of the detection system was better than 40 meV using a 21.22 eV photons from a He discharge source (SPECS UVS35/10), although, since the measurement is performed at RT, the resolution is limited by thermal effects and is about 100 meV.

STM Characterization: After MoTe₂ films growth, the samples were transferred to the STM (OMICRON) chamber without breaking the vacuum for in situ STM characterization. STM images were obtained in UHV conditions (base pressure $\approx 10^{-9}$ mbar) at room temperature using a Pt/Ir tip at the following conditions: $V = 0.1$ mV, $I = 1$ nA for high resolution images (Figure 2e–h) and $V = 0.4$ mV, $I = 400$ pA for the rest.

STEM Characterization: STEM measurements have been carried out using a Cs-corrected FEI Themis at 200 keV. HAADF-STEM images were acquired using a convergence semiangle of 18 mrad and collecting scattering >65 mrad. STEM specimens were prepared by the FIB lift-out technique using an FEI dual-beam Strata 400S at 30 kV.

Synchrotron GIXD Measurements: Diffraction measurements were performed at the European Synchrotron Radiation Facility by means of the UHV-MBE CVD diffractometer installed at the BM32 CRG/IF beamline and optimized for GIXD. The experimental setup energy and incident angle were set at 11 keV (1.13) and 0.2°, the latter set slightly below the critical angle value for total reflection in order to enhance the 2D film signal while minimizing the background.

First-Principles Calculation: The first-principles calculations were performed using the Vienna Ab initio Simulation Package^[42,43] and projector-augmented waves.^[44] The generalized-gradient approximation with Perdew–Burke–Ernzerhof^[45] parameterization was used as exchange correlation functional. The kinetic energy cutoff was set at 450 eV, using

the Monkhorst–Pack scheme^[46] employing a $12 \times 10 \times 6$ *k*-point mesh for bulk calculations. The experimental lattice constants were used and the atomic positions were fully optimized by conjugate gradient, using a force threshold of 1×10^{-3} eV Å⁻¹. Van der Waals corrections were used by applying the semiempirical DFT-D3 Grimme's method.^[47] The Maximally-Localized Wannier functions are fitted based on Mo's *s* and *d* and Te's *p* orbitals using the Wannier90 code^[48] and the surface states, topological Fermi arcs, and Weyl points calculations were carried out by the WannierTools software.^[49] Spin–orbit coupling was included in band structure calculations.

Supporting Information

Supporting Information is available from the Wiley Online Library or from the author.

Acknowledgements

This work was financially supported by the LANE Chair of Excellence program of U. Grenoble Alpes and CEA (A.D.), the Greek State Scholarships Foundation (IKY) Program for the strengthening of postdoctoral research (P.T.), the French state funds ANR-10-LABX-51-01 (Labex LANE du Programmed'Investissementsd'Avenir) and Equipex ANR-11-EQPX-0010 (G.R.). The authors thank Dr. T. Baron of Université Grenoble Alpes, CNRS, CEA/LetiMinatex, LTM for providing us with the InAs/Si substrates. The authors thank Dr. A. Kontos of INN/NCSRD for his support in the structural characterization.

Conflict of Interest

The authors declare no conflict of interest.

Keywords

2D materials, molecular beam epitaxy, orthorhombic MoTe₂, transmission electron microscopy, Weyl semimetal

Received: March 23, 2018

Revised: May 3, 2018

Published online:

- [1] S. Manzeli, D. Ovchinnikov, D. Pasquier, O. V. Yazyev, A. Kis, *Nat. Rev. Mater.* **2017**, 2, 17033.
- [2] W. Choi, N. Choudhary, G. H. Han, J. Park, D. Akinwande, Y. H. Lee, *Mater. Today* **2017**, 20, 116.
- [3] D. L. Duong, S. J. Yun, Y. H. Lee, *ACS Nano* **2017**, 11, 11803.
- [4] H. Yang, S. W. Kim, M. Chhowalla, Y. H. Lee, *Nat. Phys.* **2017**, 13, 931.
- [5] K.-A. N. Duerloo, Y. Li, E. J. Reed, *Nat. Commun.* **2014**, 5, 4214.
- [6] R. Sankar, G. N. Rao, I. P. Muthuselvam, C. Butler, N. Kumar, G. S. Murugan, C. Shekhar, T.-R. Chang, C.-Y. Wen, C.-W. Chen, W.-L. Lee, M.-T. Lin, H.-T. Jeng, C. Felser, F. C. Chou, *Chem. Mater.* **2017**, 29, 699.
- [7] Y. Qi, P. G. Naumov, M. N. Ali, C. R. Rajamathi, W. Schnelle, O. Barkalov, M. Hanfland, S.-C. Wu, C. Shekhar, Y. Sun, V. Süs, M. Schmidt, U. Schwarz, E. Pippel, P. Werner, R. Hillebrand, T. Förster, E. Kampert, S. Parkin, R. J. Cava, C. Felser, B. Yan, S. A. Medvedev, *Nat. Commun.* **2017**, 7, 11038.
- [8] A. Tamai, Q. S. Wu, I. Cucchi, F. Y. Bruno, S. Riccò, T. K. Kim, M. Hoesch, C. Barreteau, E. Giannini, C. Besnard, A. A. Soluyanov, F. Baumberger, *Phys. Rev. X* **2016**, 6, 031021.

- [9] J. Jiang, Z. K. Liu, Y. Sun, H. F. Yang, C. R. Rajamathi, Y. P. Qi, L. X. Yang, C. Chen, H. Peng, C.-C. Hwang, S. Z. Sun, S.-K. Mo, I. Vobornik, J. Fujii, S. S. P. Parkin, C. Felser, B. K. Yan, Y. L. Chen, *Nat. Commun.* **2017**, *8*, 13973.
- [10] J. Seok, J.-H. Lee, S. Cho, B. Ji, H. W. Kim, M. Kwon, D. Kim, Y.-M. Kim, S. H. Oh, S. W. Kim, Y. L. Lee, Y.-W. Son, H. Yang, *2D Mater.* **2017**, *4*, 025061.
- [11] S. Song, D. H. Keum, S. Cho, D. Perello, Y. Kim, Y. Lee, *Nano Lett.* **2015**, *16*, 188.
- [12] Y. Wang, J. Xiao, H. Zhu, Y. Alsaied, K. Y. Fong, Y. Zhou, S. Wang, W. Shi, Y. Wang, A. Zettl, E. J. Reed, X. Zhang, *Nature* **2017**, *550*, 487.
- [13] X. Qian, J. Liu, L. Fu, J. Li, *Science* **2014**, *346*, 1344.
- [14] S. Tang, C. Zhang, D. Wong, Z. Pedramrazi, H.-Z. Tsai, C. Jia, B. Moritz, M. Claassen, H. Ryu, S. Kahn, J. Jiang, H. Yan, M. Hashimoto, D. Lu, R. G. Moore, C.-C. Hwang, C. Hwang, Z. Hussain, Y. Chen, M. M. Ugeda, Z. Liu, X. Xie, T. P. Devereaux, M. F. Crommie, S.-K. Mo, Z.-X. Shen, *Nat. Phys.* **2017**, *13*, 683.
- [15] A. A. Soluyanov, D. Gresch, Z. Wang, Q. S. Wu, M. Troyer, X. Dai, B. A. Bernevig, *Nature* **2015**, *527*, 495.
- [16] Y. Wu, D. Mou, N. H. Jo, K. Sun, L. Huang, S. L. Bud'ko, C. Canfield, A. Kaminski, *Phys. Rev. B* **2016**, *94*, 121113 (R).
- [17] D. H. Keum, S. Cho, J. H. Kim, D.-J. Choe, H.-J. Sung, M. Kan, H. Kang, J.-Y. Hwang, S. W. Kim, H. Yang, K. J. Chang, Y. H. Lee, *Nat. Phys.* **2015**, *11*, 482.
- [18] Y. Sun, S.-C. Wu, M. N. Ali, C. Felser, B. Yan, *Phys. Rev. B* **2015**, *92*, 161107 (R).
- [19] L. Huang, T. M. McCormick, M. Ochi, Z. Zhao, M.-T. Suzuki, R. Arita, Y. Wu, D. Mou, H. Cao, J. Yan, N. Trivedi, A. Kaminski, *Nat. Mater.* **2016**, *15*, 1155.
- [20] K. Deng, G. Wan, P. Deng, K. Zhang, S. Ding, E. Wang, M. Yan, H. Huang, H. Zhang, Z. Xu, J. Denlinger, A. Fedorov, H. Yang, W. Duan, H. Yao, Y. Wu, S. Fan, H. Zhang, X. Chen, S. Zhou, *Nat. Phys.* **2016**, *12*, 1105.
- [21] H.-J. Kim, S.-H. Kang, I. Hamada, Y.-W. Son, *Phys. Rev. B* **2017**, *95*, 180101 (R).
- [22] A. Crepaldi, G. Autès, G. Gatti, S. Roth, A. Sterzi, G. Manzoni, M. Zacchigna, C. Cacho, R. T. Chapman, E. Springate, E. A. Seddon, Ph. Bugnon, A. Magrez, H. Berger, I. Vobornik, M. Kalläne, A. Quer, K. Rossnagel, F. Parmigiani, O. V. Yazyev, M. Grioni, *Phys. Rev. B* **2017**, *96*, 241408 (R).
- [23] Z. Wang, D. Gresch, A. A. Soluyanov, W. Xie, S. Kushwaha, X. Dai, M. Troyer, R. J. Cava, B. A. Bernevig, *Phys. Rev. Lett.* **2016**, *117*, 56805.
- [24] F. Y. Bruno, A. Tamai, Q. S. Wu, I. Cucchi, C. Barreteau, A. de la Torre, S. M. Walker, S. Riccò, Z. Wang, T. K. Kim, M. Hoesch, M. Shi, N. C. Plumb, E. Giannini, A. A. Soluyanov, F. Baumberger, *Phys. Rev. B* **2016**, *94*, 121112 (R).
- [25] C. Wang, Y. Zhang, J. Huang, S. Nie, G. Liu, A. Liang, Y. Zhang, B. Shen, J. Liu, C. Hu, Y. Ding, D. Liu, Y. Hu, S. He, L. Zhao, L. Yu, J. Hu, J. Wei, Z. Mao, Y. Shi, X. Jia, F. Zhang, S. Zhang, F. Yang, Z. Wang, Q. Peng, H. Weng, X. Dai, Z. Fang, Z. Xu, C. Chen, X. J. Zhou, *Phys. Rev. B* **2016**, *94*, 241119 (R).
- [26] I. Belopolski, D. S. Sanchez, Y. Ishida, X. Pan, P. Yu, S.-Y. Xu, G. Chang, T.-R. Chang, H. Zheng, N. Alidoust, G. Bian, M. Neupane, S.-M. Huang, C.-C. Lee, Y. Song, H. Bu, G. Wang, S. Li, G. Eda, H.-T. Jeng, T. Kondo, H. Lin, Z. Liu, F. Song, S. Shin, M. Z. Hasan, *Nat. Commun.* **2016**, *7*, 13643.
- [27] I. Belopolski, S.-Y. Xu, Y. Ishida, X. Pan, P. Yu, D. S. Sanchez, H. Zheng, M. Neupane, N. Alidoust, G. Chang, T.-R. Chang, Y. Wu, G. Bian, S.-M. Huang, C.-C. Lee, D. Mou, L. Huang, Y. Song, B. Wang, G. Wang, Y.-W. Yeh, N. Yao, J. E. Rault, P. L. Fevre, F. Bertran, H.-T. Jeng, T. Kondo, A. Kaminski, H. Lin, Z. Liu, F. Song, S. Shin, M. Z. Hasan, *Phys. Rev. B* **2016**, *94*, 085127.
- [28] L. Zhu, K. Xu, A. Zubair, A. D. Liao, W. Fang, F. Ouyang, Y.-H. Lee, K. Ueno, R. Saito, T. Palacios, J. Kong, M. S. Dresselhaus, *J. Am. Chem. Soc.* **2015**, *137*, 11892.
- [29] C. H. Naylor, W. M. Parkin, J. Ping, Z. Gao, Y. R. Zhou, Y. Kim, F. Streller, R. W. Carpick, A. M. Rappe, M. Drndić, J. M. Kikkawa, A. T. C. Johnson, *Nano Lett.* **2016**, *16*, 4297.
- [30] T. A. Empante, Y. Zhou, V. Klee, A. E. Nguyen, I.-H. Lu, M. D. Valentin, S. A. N. Alvilhar, E. Preciado, A. J. Berges, C. S. Merida, M. Gomez, S. Bobek, M. Isarraraz, E. J. Reed, L. Bartels, *ACS Nano* **2016**, *11*, 900.
- [31] L. A. Walsh, R. Yue, Q. Wang, A. T. Barton, R. Addou, C. M. Smyth, H. Zhu, J. Kim, L. Colombo, M. J. Kim, R. M. Wallace, C. L. Hinkle, *2D Mater.* **2017**, *4*, 025044.
- [32] H. C. Diaz, R. Chaghi, Y. Ma, M. Batzill, *2D Mater.* **2015**, *2*, 044010.
- [33] A. Roy, H. C. P. Movva, B. Satpati, K. Kim, R. Dey, A. Rai, T. Pramanik, S. Guchhait, E. Tutuc, S. K. Banerjee, *ACS Appl. Mater. Interfaces* **2016**, *8*, 7396.
- [34] S. Vishwanath, A. Sundar, X. Liu, A. Azcatl, E. Lochocki, A. R. Woll, S. Rouvimov, W. S. Hwang, N. Lu, X. Peng, H.-H. Lien, J. Weisenberger, S. McDonnell, M. J. Kim, M. Dobrowolska, J. K. Furdyna, K. Shen, R. M. Wallace, D. Jena, H. G. Xing, *J. Cryst. Growth* **2018**, *482*, 61.
- [35] Y. Yu, G. Wang, S. Qin, N. Wu, Z. Wang, K. He, X.-A. Zhang, *Carbon* **2017**, *115*, 256.
- [36] S. Tang, C. Zhang, C. Jia, H. Ryu, C. Hwang, M. Hashimoto, D. Lu, Z. Liu, T. P. Devereaux, Z.-X. Shen, S.-K. Mo, *APL Mater.* **2018**, *6*, 026601.
- [37] D. Rhodes, D. A. Chenet, B. E. Janicek, C. Nyby, Y. Lin, W. Jin, D. Edelberg, E. Mannebach, N. Finney, A. Antony, T. Schiros, T. Klarr, A. Mazzoni, M. Chin, Y.-C. Chiu, W. Zheng, Q. R. Zhang, F. Ernst, J. I. Dadap, X. Tong, J. Ma, R. Lou, S. Wang, T. Qian, H. Ding, R. M. Osgood Jr., D. W. Paley, A. M. Lindenberg, P. Y. Huang, A. N. Pasupathy, M. Dubey, J. Hone, L. Balicas, *Nano Lett.* **2017**, *17*, 1616.
- [38] R. He, S. Zhong, H. H. Kim, G. Ye, Z. Ye, L. Winford, D. McHaffie, I. Rilak, F. Chen, X. Luo, Y. Sun, A. W. Tsen, *Phys. Rev. B* **2018**, *97*, 041410 (R).
- [39] P. Tsipas, D. Tsoutsou, S. Fragkos, R. Sant, C. Alvarez, H. Okuno, G. Renaud, R. Alcotte, T. Baron, A. Dimoulas, *ACS Nano* **2018**, *12*, 1696.
- [40] L. Ö. Olsson, C. B. M. Andersson, M. C. Håkansson, J. Kanski, L. Ilver, U. O. Karlsson, *Phys. Rev. Lett.* **1996**, *76*, 3626.
- [41] A. Tagushi, K. Kanisawa, *Appl. Surf. Sci.* **2006**, *252*, 5263.
- [42] G. Kresse, J. Furthmüller, *Comput. Mater. Sci.* **1996**, *6*, 15.
- [43] G. Kresse, J. Furthmüller, *Phys. Rev. B* **1996**, *54*, 11169.
- [44] P. E. Blöchl, *Phys. Rev. B* **1994**, *50*, 17953.
- [45] J. P. Perdew, K. Burke, M. Ernzerhof, *Phys. Rev. Lett.* **1996**, *77*, 3865.
- [46] H. Monkhorst, J. Pack, *Phys. Rev. B* **1976**, *13*, 5188.
- [47] S. Grimme, J. Antony, S. Ehrlich, S. A. Krieg, *J. Chem. Phys.* **2010**, *132*, 154104.
- [48] A. A. Mostofi, J. R. Yates, Y.-S. Lee, I. Souza, D. Vanderbilt, N. Marzari, *Comput. Phys. Commun.* **2014**, *185*, 2309.
- [49] Q. S. Wu, S. N. Zhang, H.-F. Song, M. Troyer, A. A. Soluyanov, *Comput. Phys. Commun.* **2018**, *224*, 405.

Reprint Order Form 2018

Short DOI: **adfm.** _____

Please send me and bill me for

☐

Reprints via ☐ airmail (+ 25 Euro)
☐ surface mail

Please send me and bill me for a:

☐

Issue copies (25 Euro)

☐

high-resolution PDF file (330 Euro).

My Email address: _____

Please note: It is not permitted to present the PDF file on the internet or on company homepages.

Information regarding VAT

Please note that from German sales tax point of view, the charge for **Reprints, Issues or Posters** is considered as “supply of goods” and therefore, in general, such delivery is a subject to German sales tax. However, this regulation has no impact on customers located outside of the European Union. Deliveries to customers outside the Community are automatically tax-exempt. Deliveries within the Community to institutional customers outside of Germany are exempted from the German tax (VAT) only if the customer provides the supplier with his/her VAT number. The VAT number (value added tax identification number) is a tax registration number used in the countries of the European Union to identify corporate entities doing business there. It starts with a country code (e.g. FR for France, GB for Great Britain) and follows by numbers.

VAT no.: _____

(Institutes / companies in EU countries only)

Purchase Order No.: _____

Delivery address / Invoice address:

Name of recipient, University, Institute, Street name and Street number, Postal Code, Country

Date and Signature: _____

Credit Card Payment (optional) -You will receive an invoice.

VISA, MasterCard, AMERICAN EXPRESS

Please use the Credit Card Token Generator located at the website below to create a token for secure payment. The token will be used instead of your credit card number.

Credit Card Token Generator:

https://www.wiley-vch.de/editorial_production/index.php

Please transfer your token number to the space below.

Credit Card Token Number

| | | | | | | | | | | | | | | | | | | | |
|--|--|--|--|--|--|--|--|--|--|--|--|--|--|--|--|--|--|--|--|
| | | | | | | | | | | | | | | | | | | | |
|--|--|--|--|--|--|--|--|--|--|--|--|--|--|--|--|--|--|--|--|

Price list for reprints (The prices include mailing and handling charges. All Wiley-VCH prices are exclusive of VAT)

| No. of pages | 50 copies | 100 copies | 150 copies | 200 copies | 300 copies | 500 copies |
|------------------------------|-----------|------------|------------|------------|------------|------------|
| 1-4 | 345 | 395 | 425 | 445 | 548 | 752 |
| 5-8 | 490 | 573 | 608 | 636 | 784 | 1077 |
| 9-12 | 640 | 739 | 786 | 824 | 1016 | 1396 |
| 13-16 | 780 | 900 | 958 | 1004 | 1237 | 1701 |
| 17-20 | 930 | 1070 | 1138 | 1196 | 1489 | 2022 |
| for every additional 4 pages | 147 | 169 | 175 | 188 | 231 | 315 |